Pol. J. Environ. Stud. Vol. XX, No. X (XXXX), 1-15

DOI: *10.15244/pjoes/220960* ONLINE PUBLICATION DATE: 2026-09-18

Original Research

Research on the Inversion Method of Total Phosphorus Concentration in Water Bodies Based on PSO-Adam-BP Neural Network Model

Guanxing Wang[1, 2], Cui Jia[1, 2], Linghan Gao[1, 2]*, Shan An[1, 2], Jia Xi[1, 2], Yaxue Liu[3]

[1]School of Remote Sensing and Information Engineering, North China Institute of Aerospace Engineering, Langfang 065000, China

[2]Hebei Collaborative Innovation Center for Aerospace Remote Sensing Information Processing and Application, Langfang 065000, China

[3]Hebei PetroChina Central Hospital, Langfang 065000, China

Received: 15 January 2026
Accepted: 21 April 2026

Abstract

This study investigated Baiyangdian Lake in the Xiong'an New Area to invert total phosphorus (TP) concentrations using Sentinel-2 multispectral imagery and in situ measurements, aiming to support water-quality assessment and eutrophication management. Based on the multispectral remote sensing data of Sentinel-2 and measured total phosphorus data of water bodies, the study used specific feature combinations such as NDTI, B5, B11-B12 difference, and sensitive combination bands of measured data as model inputs to construct a PSO-Adam-BP neural network machine learning model for total phosphorus concentration inversion. Compared with the traditional BP and PSO-BP baseline models, the proposed framework significantly improved the accuracy of the model, with an R^2 value reaching 0.9351. Moreover, it successfully reduced the average relative error by up to 53.5%, from 4.80% to 2.24%, and decreased the maximum relative error by up to 31.7%, from 11.21% to 7.66%, demonstrating the model's highly robust and precise inversion performance. This study provides a new method for water quality detection in Baiyangdian Lake and is of great significance to the protection and development of the water environment in Xiong'an New Area.

Keywords: Baiyangdian Lake, total phosphorus inversion, PSO-Adam-BP Model, water quality monitoring, Sentinel-2

Introduction

Water is a vital natural resource, but it is experiencing depletion, pollution, and poor management. According to the 2020 Global Risk Report, water crises, including water shortage, water pollution, and other water problems, rank fifth among the top ten risks with the greatest impact, especially water pollution. Among water pollution, eutrophication is a relatively common phenomenon [1]. "Water bloom" is a serious water environment problem caused by eutrophication of water bodies. It hinders the normal

*e-mail: gaolh@nciae.edu.cn
0000-0002-8537-8787

growth of aquatic organisms and pollutes the drinking water sources of residents, which has a direct impact on people's daily life and production activities [2]. Phosphorus, as a key biogenic element for maintaining primary productivity in aquatic ecosystems, is an important indicator for measuring the degree of water pollution and eutrophication of water bodies [3, 4]. However, excessive P flow from agricultural fertilizers and untreated wastewater into aquatic ecosystems poses a severe threat. Over a period of time, if the concentration of phosphorus increases too quickly (e.g., exceeding the normal range of 0.05-0.08 mg/L), it will cause microorganisms such as cyanobacteria in the water body to grow rapidly, which will lead to an imbalance of microorganisms in the water body and cause water bloom and long-term eutrophication [5]. This change process destroys the ecological balance of the water body [6, 7]. In view of this, the detection and analysis of total phosphorus in water bodies is of critical significance for water environment management and ecological protection practices.

The traditional water quality monitoring method is to manually take samples from the water and then conduct laboratory analysis. This method may not be as efficient as expected for large-scale detection [8]. With the rapid development of remote sensing technology, the study of water quality in large-area water bodies has been greatly promoted. Water quality remote sensing monitoring technology is based on remote sensing images and can monitor large-scale water bodies, overcoming the shortcomings of traditional point observations and providing technical support for large-area and multi-time span water body monitoring and water quality parameter inversion [9]. By establishing an inversion model between spectral reflectivity and water quality parameter concentrations, it is possible to achieve large-scale and rapid estimation of water quality indicators [10]. Among them, remote sensing water quality parameter inversion methods mainly include empirical methods, semi-empirical/semi-analytical methods, analytical methods (physical model methods) and machine learning methods. The advantage of machine learning is that it can automatically mine the complex nonlinear relationship between spectral data and water quality parameters, without the need for preset function forms, and can process high-dimensional features. It has higher inversion accuracy for complex eutrophic water bodies [11, 12]. In order to further accurately invert water quality parameters and improve the accuracy and applicability of models, the integrated application of machine learning and remote sensing technology has become the core direction of current research.

In the field of total phosphorus (TP) inversion research, a variety of modeling approaches have been explored with notable progress. Early studies primarily relied on basic spatial interpolation and semi-linear regression models. For instance, Liang Yongchun et al. [13] utilized inverse distance weighting (IDW) to map TP concentrations in Taihu Lake. Similarly, researchers such as Zheng Shuilin et al. [14] and Song Kaishan et al. [15] successfully applied adaptive partial least squares (PLS) and GA-PLS models to typical urban water bodies and reservoirs. Despite achieving high inversion accuracy in these relatively homogeneous aquatic environments, such fundamentally semi-linear projections are insufficient for Baiyangdian Lake. As a typical shallow, macrophyte-dominated lake, Baiyangdian Lake suffers from severe bottom and vegetation optical interference, making the mapping between TP and spectral variables highly complex and profoundly non-linear. To address these non-linear complexities, advanced machine learning models have been increasingly adopted. Zhou Yi et al. [16] demonstrated this by utilizing a Grid Search-optimized XGBoost model combined with Sentinel-2 imagery to achieve superior TP prediction in East Juyan Lake. Furthermore, Sun Zhihao et al. [17] employed a multilayer denoising autoencoder combined with ensemble learning to extract effective spectral features, significantly boosting the R^2 of their model from 0.62 to 0.90. While these modern hybrid approaches exhibit excellent predictive capabilities, standard artificial neural networks (ANNs) – particularly the Back Propagation (BP) model – remain highly attractive due to their universal ability to approximate complex non-linear functions without requiring preset mathematical forms. However, when applied to high-dimensional, highly redundant, and noisy multispectral satellite data, basic BP networks exhibit critical bottlenecks. They are highly susceptible to becoming trapped in local optima during gradient descent and often suffer from exceedingly slow convergence rates, severely limiting their practical robustness and precision.

Sentinel-2 multispectral data has the characteristics of high dimensionality, strong redundancy between bands, and a complex nonlinear relationship with total phosphorus concentration and spectral response. The images of some substances in the water spectral signal, such as suspended solids and algae, show strong nonlinear and multivariate coupling characteristics in total phosphorus inversion. Traditional empirical models and general machine learning methods are difficult to accurately describe this complex relationship [18]. In response to the above problems, this study optimizes the algorithm based on traditional machine learning in order to improve the accuracy of the model in complex optical environments like Baiyangdian Lake. First, this paper proposes a method for inverting total phosphorus concentration in water based on particle swarm optimization-Adam-back propagation neural network (PSO-Adam-BP). The model is based on a BP neural network and combines the hybrid optimization strategy of PSO global optimization + Adam local gradient fine-tuning to avoid the problem of falling into local optimality when BP neural network is used alone [19], fundamentally overcoming the optimization bottlenecks of standard neural networks and endowing the model with superior non-linear feature-extraction capabilities. Secondly, when inputting the model, characteristic parameters with high correlation with total phosphorus concentration in water bodies were constructed based on Sentinel-2 data, such as NDTI, NDWI, B5/B6 ratio, B11-B12 combination and other multi-source features. At the same time, a data enhancement mechanism of random noise perturbation and spectral scaling was introduced to improve the generalization ability of the model under small sample conditions. By addressing the specific non-linear complexities of macrophyte-dominated lakes, the proposed PSO-Adam-BP framework achieves a quantified breakthrough over the conventional baselines discussed in [12-16]. Specifically, it yields a highly robust R^2 of 0.9351 and reduces the average relative error by up to 53.5% compared to standard neural networks. This marked improvement highlights the methodological novelty of our dual-optimization strategy and offers a highly reliable tool for complex aquatic environments.

Materials and Methods

Study Area

Baiyangdian Lake (38°44'~38°59'N, 115°45'~116°06'E) is a famous freshwater lake wetland in northern China. It is located in the central part of Hebei Province, mainly across the two cities of Baoding and Cangzhou, involving Anxin, Xiongxian, Rongcheng, Renqiu and other districts and counties. It has a total area of 366 km^2 and consists of 143 interconnected large and small lakes [20]. It is the largest freshwater lake group on the North China Plain. Due to its special terrain and geographical environment, Baiyangdian Lake has a small net flow, slow flow rate, poor self-purification ability, small environmental capacity, and is easily polluted, resulting in prominent nitrogen and phosphorus pollution in the water body [21, 22], which in turn causes eutrophication of the water body. Historically, the annual TP concentration in Baiyangdian Lake fluctuated around 0.2 mg/L, classifying the water quality as Grade V or worse [23]. Quantitative source apportionment indicates that agricultural and rural non-point sources are the primary drivers, contributing approximately 73.37% to the TP load, compounded by domestic sewage discharged from upstream urban areas [24]. However, following the establishment of the Xiong'an New Area in 2017, intensive ecological restoration and water diversion projects were implemented. As a result, the water quality of Baiyangdian Lake has significantly improved, successfully reaching the Grade III standard ($TP \leq 0.05$ mg/L) since 2021 [25]. The location of the study area is shown in Fig. 1.

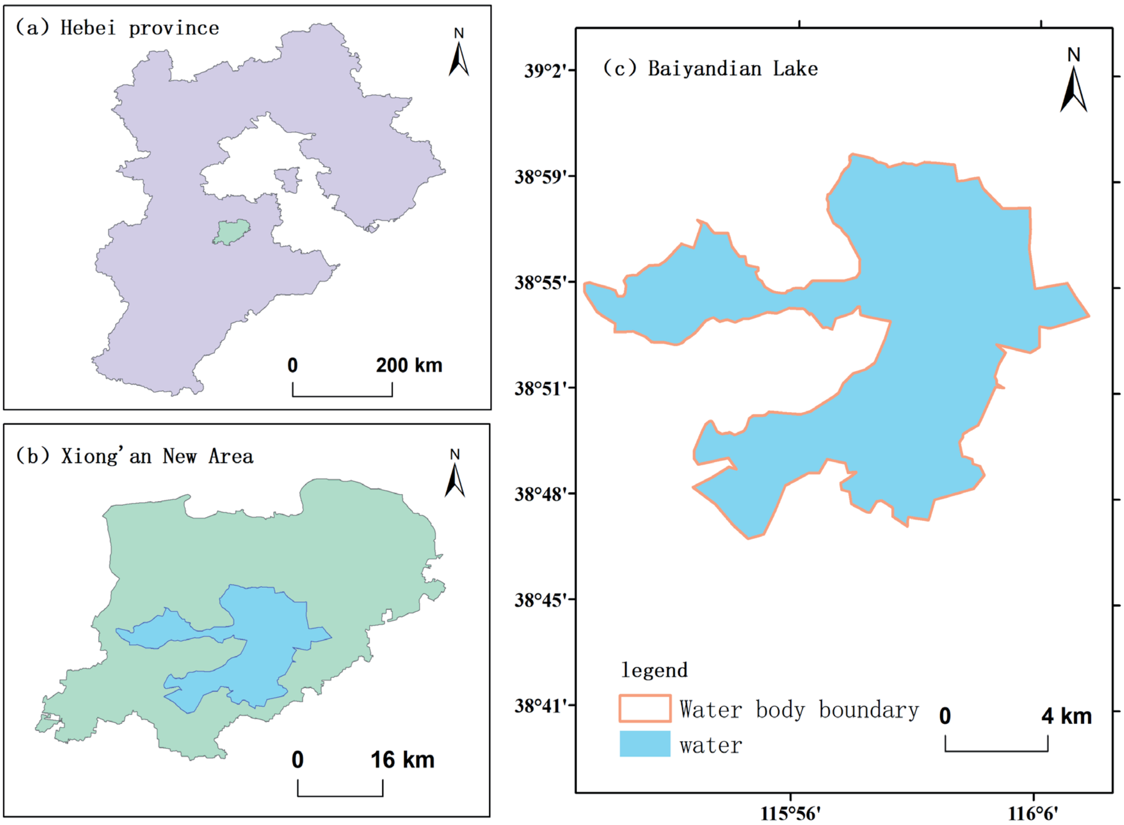

Fig. 1. Location map of the study area. a) Hebei Province, b) Xiongan New Area, c) Baiyangdian Lake.

Experimental data

Measured Data Acquisition

In May 2025, data collection was conducted in the northern part of Baiyangdian Lake. The time window for matching ground-based data and remote sensing images was ±7 days [26, 27]. A total of 40 points were collected. To ensure statistical independence and mitigate spatial autocorrelation (e.g., Moran's I), these in situ sampling points were strategically deployed across heterogeneous regions with sufficient spatial intervals. Maintaining an adequate geographic distance between sample locations is a widely recognized spatial sampling strategy to effectively reduce spatial autocorrelation and local data redundancy [28]. GPS positioning was performed using an Ovimap, and surface spectra were measured using a water surface spectrometer based on the above-water measurement method to collect water spectra at the corresponding points [29]. The weather was clear and cloudless when the data was collected, and the water surface was calm. The distribution of water sampling points is shown in Fig. 2.

The measured values of some sampling points are shown in Table 1.

Table 1. Some measured sampling data.

Point	Measured value (mg/L)	Point	Measured value (mg/L)
1	0.033	11	0.026
2	0.036	12	0.026
3	0.029	13	0.027
4	0.034	14	0.031
5	0.026	15	0.03
6	0.031	16	0.029
7	0.031	17	0.033
8	0.034	18	0.031
9	0.03	19	0.038
10	0.027	20	0.03

Remote Sensing Image Acquisition and Preprocessing

This study used Sentinel-2 Level-2A surface reflectance products from the European Space Agency. Sentinel-2 images have a spatial resolution of 10 m, cover the spectral range of 0.4 to 2.4 μm in 13 bands, and span the visible, near-infrared, and shortwave infrared regions. Their revisit time is approximately five days, meeting the requirements of this experiment.

Atmospheric correction, resampling, band fusion, image cropping, and other preprocessing operations were performed using the Sen2Cor processor [30] to obtain the required remote sensing data of the study area. Secondly, feature parameters were extracted based on the processed images to construct feature parameters with high correlation with the total

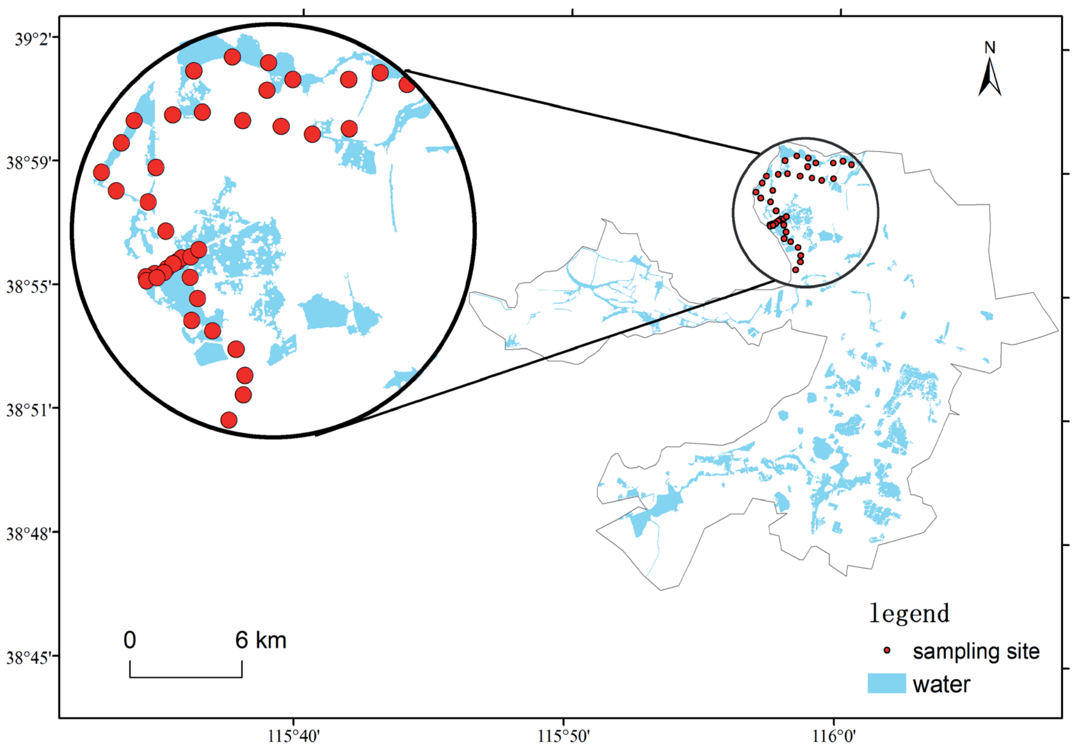

Fig. 2. Sampling point distribution.

phosphorus concentration value of the water body. Finally, to address the limited number of in situ samples and prevent the neural network from overfitting, data augmentation was performed by adding zero-mean Gaussian noise, increasing the dataset from 40 to 120 samples. This is a well-established technique in water quality remote sensing for overcoming small dataset limitations [31]. The standard deviation (σ) of the injected noise was strictly restricted to 5% of the original sample values. This threshold is scientifically justified as it aligns precisely with the inherent surface reflectance radiometric uncertainty of the Sentinel-2 multispectral sensor [32]. Statistical tests confirmed that this augmented dataset effectively preserved the real-world probability density distribution of the original samples without introducing artificial systemic bias. The dataset was then split into training and test sets at a ratio of 8:2. The above processing flow is shown in Fig. 3.

Experimental Methods

The characteristic parameters of the model input used the 12 bands of Sentinel-2 data (except B10) and constructed three combined features based on band relationships, namely NDTI, B5/B6 and B11-B12 difference. The specific calculation method of the combined features is shown in Table 2. To quantitatively and physically justify the selection of these specific features over other common indices, a Pearson correlation analysis was conducted between the spectral indices and the in situ TP concentrations. As TP is a non-optically active parameter, its inversion relies on complex proxies like suspended particulate matter and phytoplankton. The statistical analysis presented in Fig. 4 revealed that NDTI, yielding a correlation coefficient of −0.24, exhibited the highest relative correlation magnitude among the evaluated indices, capturing the adsorption of phosphorus to suspended sediments. While NDWI exhibited a marginally higher linear correlation of 0.08 compared to 0.03 for B5/B6 and –0.05 for B11-B12, it was deliberately excluded from the final feature set. NDWI is primarily designed for water body delineation; its variance within an already defined aquatic zone often reflects physical depth or surface glint rather than true nutrient dynamics. Conversely, B5/B6 and B11-B12 were retained based on fundamental optical mechanisms: the red-edge ratio of B5 to B6 serves as a critical biological proxy for phytoplankton biomass driven by phosphorus enrichment, and the shortwave infrared difference between B11 and B12 effectively

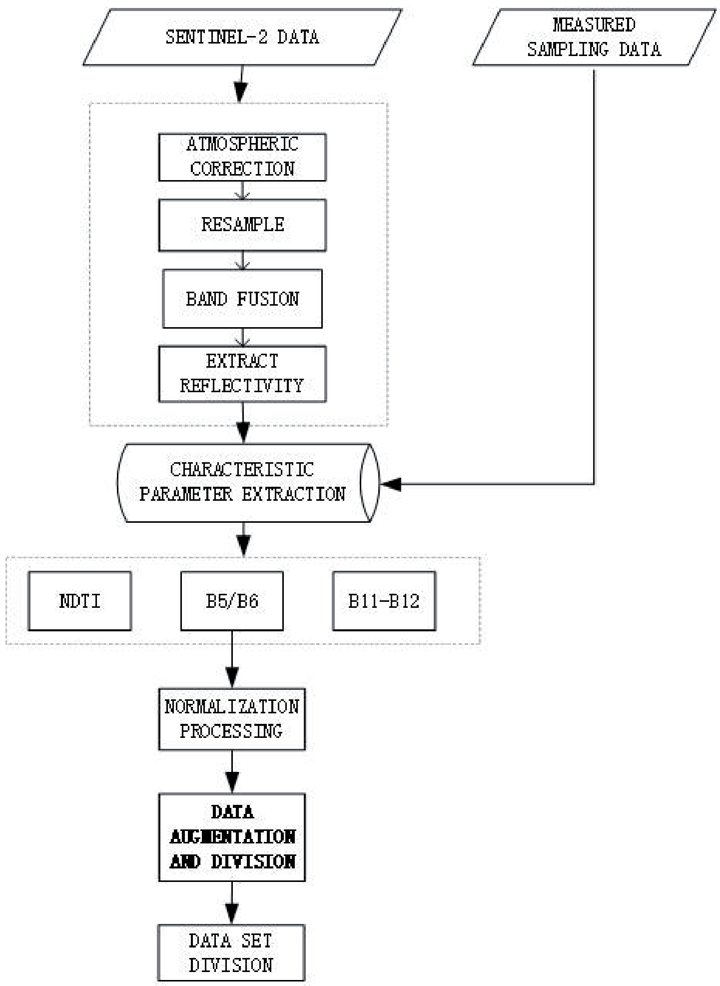

Fig. 3. Remote sensing image preprocessing.

Table 2. Feature combination.

NDTI	B5/B6 ratio	B11-B12 combination item
Turbidity index constructed based on red and green bands	The ratio of red edge 1 to red edge 2 is used to highlight the spectral differences between vegetation and water bodies, thereby increasing the sensitivity to indirect changes in total phosphorus.	Construct a linear combination through the shortwave infrared band to reduce the influence of atmospheric and background noise.

isolates water-leaving radiance by suppressing atmospheric and surface glint noise. Most importantly, the overall low linear correlation coefficients across all individual indices, with absolute values remaining below 0.30, quantitatively demonstrate that the relationship between TP and spectral reflectance in Baiyangdian Lake is highly non-linear. This fundamentally justifies the absolute necessity of employing a deep learning architecture, which is specifically designed to decode these complex, non-linear physical and biological couplings that traditional linear empirical models fail to capture.

After normalizing the aforementioned characteristic bands and the Sentinel imagery's own bands, a 15-dimensional input feature vector X = [B1, B2, …, B12, NDTI, B5/B6, B11−B12] was formed, serving as the input to the PSO-Adam-BP neural network in this experiment. The overall experimental process involved first using the particle swarm optimization (PSO) algorithm to perform a global search for the network's initial weights, aiming to minimize the initial point's proximity to the optimal solution. The optimal weights found by PSO were then loaded into the BP neural network, and the Adam algorithm was used to perform gradient fine-tuning of the parameters to achieve local convergence and improve accuracy.

After training, the predicted results of the test set were compared with the measured total phosphorus concentrations, and the model performance was evaluated using indicators such as the coefficient of determination (R^2), mean absolut error (MAE), and root mean square error (RMSE).

Model Construction and Accuracy Assessment

PSO-Adam-BP Neural Network Model Construction

(1) Construct the input training set and test set of the model. Perform Min-Max normalization on the input features and TP concentration to ensure that the features of each band are at the same scale. On this basis, the enhancement strategy of noise perturbation and scaling is introduced to generate multiple sets of perturbed samples to improve the generalization ability of the model. After data enhancement, the 120 sample data sets are divided into training set and test set in an 8:2 ratio.

(2) A multi-layer fully connected feedforward neural network was constructed. The sample set was defined as follows:

$$\{(x_i, y_i)\}_{i=1}^{m}, \quad x_i \in \mathbb{R}^n, y_i \in \mathbb{R} \tag{1}$$

Among them, x_i represents the input feature vector of the i-th sample (such as multispectral reflectance and constructed remote sensing index, etc.), y_i is the corresponding measured total phosphorus concentration value, m is the total number of samples, n is the input feature dimension, and R represents the real number set.

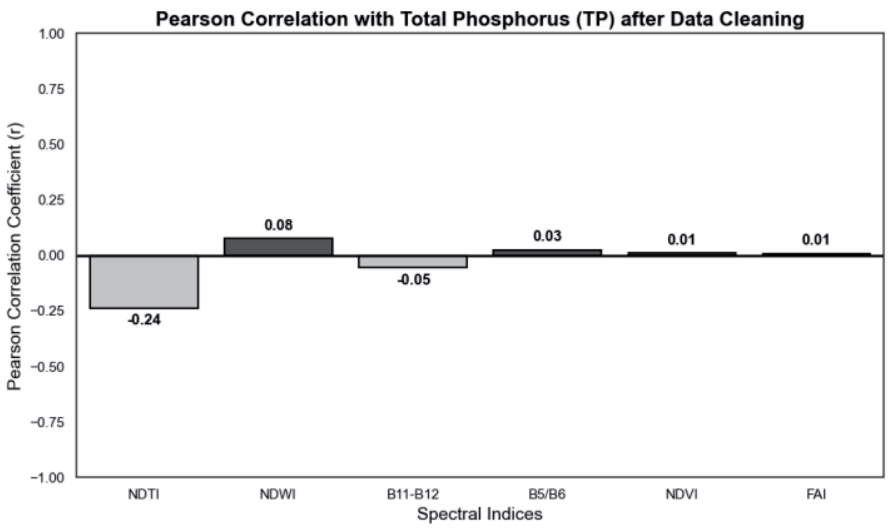

Fig. 4. Pearson correlation analysis.

The forward propagation function of the model is:

$$\hat{y} = f(x; W, b) = W_4\phi(W_3\phi(W_2\phi(W_1x + b_1) + b_2) + b_3) + b_4 \quad (2)$$

Where W_k and b_k are the weights and biases of the k-th layer, ϕ is the activation function, x is the input feature vector, and $\hat{y}$ is the predicted value. To ensure complete transparency and fair comparison across the standard BP, PSO-BP, and PSO-Adam-BP models, an identical baseline neural network architecture was utilized. The finalized topology consists of an input layer with 15 neurons, followed by 3 progressively down-sampled hidden layers containing 256, 128, and 64 neurons, respectively. The ReLU activation function was applied across all hidden layers to prevent the vanishing gradient problem. To effectively mitigate overfitting during the training phase, a Dropout layer with a rate of 0.2 was incorporated immediately after the first hidden layer. The output layer contains a single neuron for continuous TP concentration prediction.

Furthermore, to scientifically justify this topological design and ensure its optimal synergy with our hybrid optimization strategy, a rigorous sensitivity analysis was conducted directly on the proposed end-to-end PSO-Adam-BP framework, as illustrated in Fig. 5. We evaluated different neuron configurations, such as scaling the base architecture down to a 128-64-32 structure or expanding it to a 512-256-128 structure. The analysis demonstrated that the chosen 256-128-64 configuration achieved the optimal balance, maximizing the testing R^2 while minimizing the RMSE. Shallower or narrower architectures lacked the non-linear capacity to map complex optical features under the PSO-Adam optimization, inevitably leading to underfitting, whereas excessively wide networks introduced severe overfitting to training noise. Therefore, this rigorously tested 3-hidden-layer structure was established as the optimal architecture for the final model.

(3) Initial model parameter setting. Particle swarm optimization (PSO) was used to search for the global optimal solution for network weights. PSO simulates swarm intelligence, updates particle positions and velocities, and seeks the minimum value of the fitness function. The optimal result was used as the initial input of the BP model.

$$v_i^{t+1} = \omega v_i^t + c_1 r_1 (p_i - x_i^t) + c_2 r_2 (g - x_i^t)$$
$$x_i^{t+1} = x_i^t + v_i^{t+1} \quad (3)$$

Where x_i and v_i are the particle position and velocity respectively, p_i is the individual optimal solution, g is the global optimal solution, ω is the inertia weight, c_1 and c_2 are learning factors, r_1 and r_2 are random numbers in (0,1), and t represents the t-th iteration.

(4) Model parameter fine-tuning strategy. After completing the PSO global search, the optimal result weights were initialized to the BP network. During the model execution, the Adam optimizer was used to fine-tune the parameters to obtain higher accuracy. Adam achieves dynamic learning rate adjustment through adaptive first-order moment estimation and second-order moment estimation. Its parameter update formula is:

$$m_t = \beta_1 m_{t-1} + (1 - \beta_1) g_t$$
$$v_t = \beta_2 v_{t-1} + (1 - \beta_2) g_t^2$$
$$\widehat{m}_t = \frac{m_t}{1 - \beta_1^t}$$
$$\hat{v}_t = \frac{v_t}{1 - \beta_2^t}$$
$$\theta_{t+1} = \theta_t - \eta \frac{\widehat{m}_t}{\sqrt{\hat{v}_t} + \epsilon} \quad (4)$$

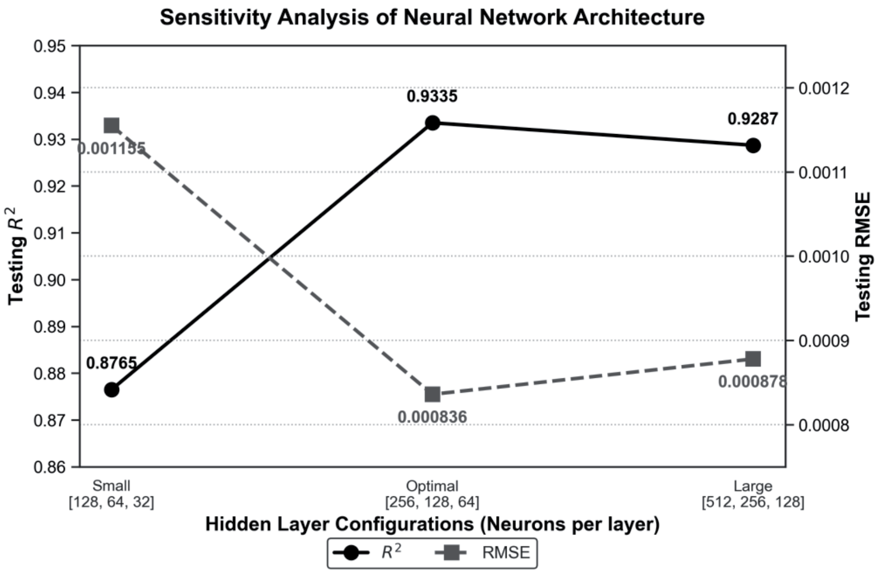

Fig. 5. Model sensitivity analysis.

Among them, θ is the network parameter, g_t is the gradient, $\widehat{m}_t$ and $\hat{v}_t$ are the first and second order moments after deviation correction.

To ensure optimal model performance and avoid arbitrary parameter selection, the hyperparameters of both the PSO and Adam algorithms were rigorously tuned. A systematic grid search strategy, combined with established empirical recommendations from deep learning literature, was employed. For the PSO algorithm, the inertia weight (ω) and learning factors (c_1, c_2) were determined via grid search within the standard theoretical convergence boundaries to balance global exploration and local exploitation. A swarm size of 100 and 300 maximum iterations was found to be the optimal trade-off between computational efficiency and convergence stability. For the Adam optimizer, the initial learning rate (η = 0.005) and the L2 regularization penalty (weight decay $\lambda = 10^{-4}$) were optimized utilizing a grid search over logarithmic scales to minimize the validation error. The exponential decay rates for the first and second-moment estimates (β_1 and β_2) were kept at their highly robust standard default values of 0.9 and 0.999, respectively. The specific hyperparameter settings used in this experiment are comprehensively detailed in Table 3.

The PSO-Adam-BP neural network model structure is shown in Fig. 6.

Accuracy Evaluation Indicators

Model performance was evaluated using the coefficient of determination (R^2), root mean square error (RMSE) and mean absolute error (MAE). The formulas are given below.

$$R^2 = 1 - \frac{\sum_{i=1}^{n}(y_{obs,i} - \hat{y}_{\mathrm{mod},i})^2}{\sum_{i=1}^{n}(y_{obs,i} - \overline{y}_{obs})^2} \tag{5}$$

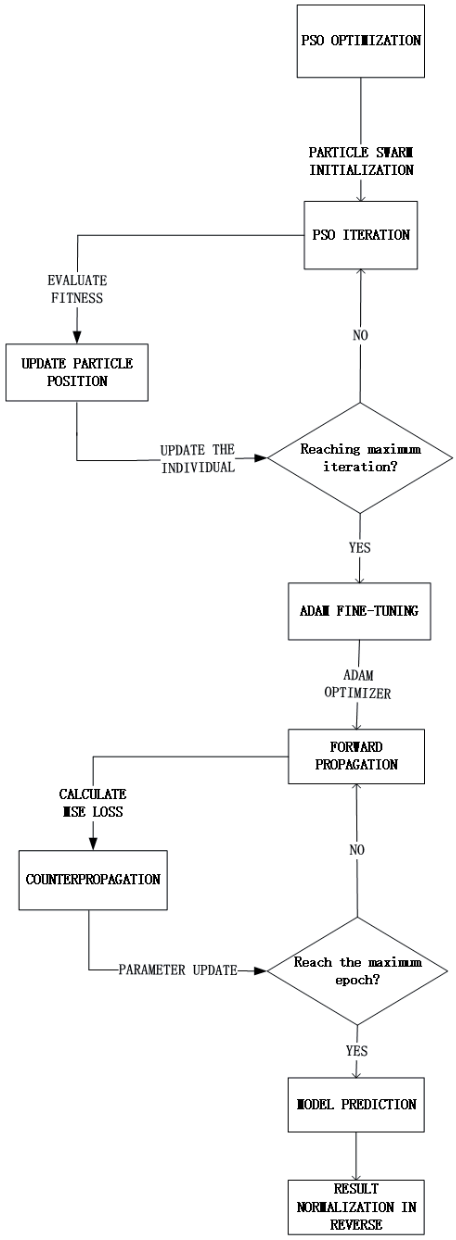

Fig. 6. Model optimization diagram.

Table 3. Hyperparameter table.

Optimizer/Algorithm	Hyperparameter	Symbol	Value	Description
PSO	Swarm size	N	100	Number of particles in the swarm
	Maximum iterations	Tmax	300	Termination criterion for global search
	Inertia weight	ω	0.9	Balances global and local exploration
	Cognitive learning factor	c_1	2	Pulls particles toward local best
	Social learning factor	c_2	2	Pulls particles toward global best
Adam & BP	Learning rate	η	0.005	Step size for gradient descent update
	Exponential decay rate 1	β_1	0.9	First-order moment estimation (momentum)
	Exponential decay rate 2	β_2	0.999	Second-order moment estimation
	L2 Regularization penalty	λ	1.00E-04	Weight decay to prevent overfitting
	Training Epochs	E	200	Total passes through the training dataset

$$MAE = \frac{1}{n}\sum_{i=1}^{n}(\mid \hat{y}_{\mathrm{mod},i} - y_{obs,i} \mid) \tag{6}$$

$$RMSE = \sqrt{\frac{\sum_{i=1}^{n}(\hat{y}_{\mathrm{mod},i} - y_{obs,i})^2}{n}} \tag{7}$$

In the above formula, $y_{obs,i}$ is the measured value of a water quality parameter of the i-th group of samples; $\overline{y}_{obs}$ is the measured average value; $\hat{y}_{mod,i}$ is the model inversion value; and n is the total number of samples.

Results and Discussion

PSO-Adam-BP Neural Network Model Inversion Results

The training and test sets of the total phosphorus concentration inversion results of the Baiyangdian Lake water body based on the PSO-Adam-BP neural network model are shown in Fig. 7. The R^2 on the test set was 0.9351, which shows that the correlation is high (R^2>0.91), indicating that the model can effectively capture the highly non-linear relationship between the multidimensional spectral features of Sentinel-2 and the TP concentration.

The loss curve generated during the model execution is shown in Fig. 8. It can be seen that the convergence is stable after about T = 75 iterations. The PSO algorithm's global search for the network's initial weights effectively avoids local optimality, and combined with Adam's gradient fine-tuning, it achieves rapid convergence of parameters.

From the perspective of relative error analysis, the model's average relative error on the test set was 2.24%. Approximately 79.2% of the samples had relative errors less than 3%, with 25.0% falling within the 1%-2% range. The maximum relative error was 7.66%, and the minimum error was 0.49%. This demonstrates that the model exhibits high accuracy and good stability in retrieving total phosphorus concentration in water bodies. The model's relative error results are shown in Table 4.

Comparison of Model Inversion Results

In order to further study the performance of the PSO-Adam-BP model, the following two comparative models were established:

(1) Unoptimized BP neural network. To ensure a strict and fair ablation study, the standard BP model

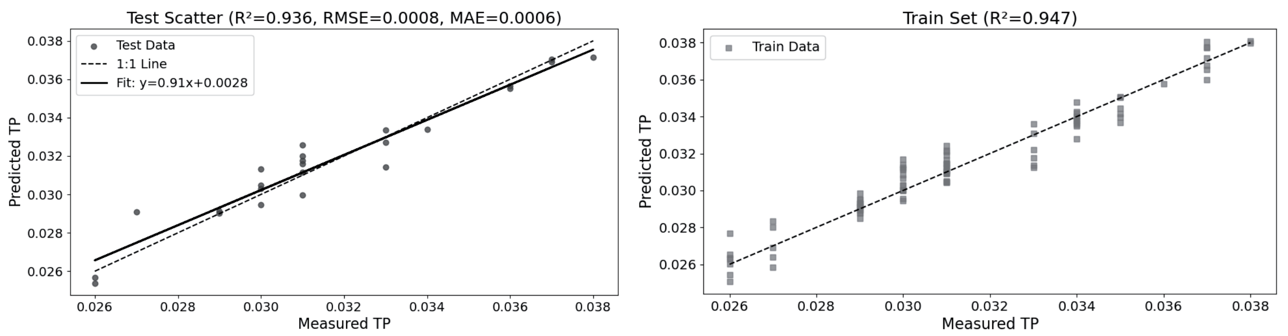

Fig. 7. Fitting curves of the training set (right) and test set (left).

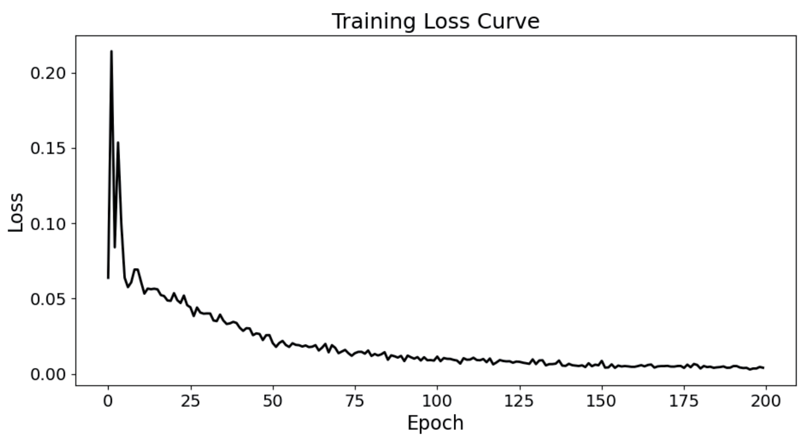

Fig. 8. Loss function curve.

Table 4. Model relative error results.

	PSO-Adam-BP		
ID	Measured value (mg/L)	Predicted value (mg/L)	Relative error (%)
1	0.030999999	0.0319	2.85%
2	0.033	0.032000002	3.15%
3	0.030999999	0.0307	1.00%
4	0.035999998	0.035	2.67%
5	0.030999999	0.031199999	0.58%
6	0.026000001	0.0263	1.28%
7	0.029999999	0.031300001	4.26%
8	0.027000001	0.028200001	4.47%
9	0.030999999	0.031300001	0.81%
10	0.033	0.033399999	1.29%
11	0.037	0.037599999	1.66%
12	0.037999999	0.0383	0.66%
13	0.029999999	0.0298	0.60%
14	0.030999999	0.030400001	1.82%
15	0.037	0.037300002	0.73%
16	0.029999999	0.032299999	7.66%
17	0.034000002	0.034200002	0.49%
18	0.029999999	0.0308	2.71%
19	0.028999999	0.029300001	1.15%
20	0.030999999	0.0317	2.32%
21	0.028999999	0.029300001	0.97%
22	0.035999998	0.036800001	2.33%
23	0.026000001	0.026699999	2.68%
24	0.033	0.031199999	5.50%

was trained using the identical network architecture (256-128-64) and the same Adam optimizer, but without the PSO global weight initialization.

(2) PSO-BP model optimized by PSO. This model utilized the exact same PSO global initialization as our proposed model, but the fine-tuning phase relied on the traditional Stochastic Gradient Descent (SGD) optimizer rather than the adaptive Adam.

To compare the prediction performance of different models, the prediction errors of the BP neural network, PSO-BP neural network, and PSO-Adam-BP neural network on the same 24 samples were statistically analyzed. The predicted values and relative deviations of the two models are shown in Table 5. Although the traditional BP model has a lower error on some samples, the average relative error on the test set was 4.80%, the maximum relative error was 11.21%, and the minimum error was 0.30%, indicating significant instability. Although the PSO-BP model improves the upper limit of prediction through particle swarm optimization, the average relative error on the test set was 3.47%, the maximum relative error was 9.21%, and the minimum error was 0.00%. However, the average error is still higher than that of the PSO-Adam-BP model.

Furthermore, to comprehensively evaluate the prediction performance and address absolute deviations as required for rigorous literature comparison, absolute error metrics including RMSE and MAE alongside the coefficient of determination R^2 were computed for all three models, as detailed in Table 6. As demonstrated in the ablation study, the standard BP model exhibited the poorest baseline performance with an R^2 of 0.6881 and an RMSE of 0.0018 mg/L, highlighting the difficulty of escaping local optima in complex high-dimensional feature spaces without global guidance. The introduction of PSO global optimization

Table 5. Comparison model results.

ID	Actual TP (mg/L)	BP Predicted value (mg/L)	BP Relative error (%)	PSO-BP Predicted value (mg/L)	PSO-BP Relative error (%)
1	0.030999999	0.0318	2.9032%	0.0315	1.6129%
2	0.033	0.0293	11.2121%	0.0305	7.5758%
3	0.030999999	0.0296	4.1935%	0.0307	0.9677%
4	0.035999998	0.03460	3.8889%	0.0357	0.8333%
5	0.030999999	0.0313	0.9677%	0.0308	0.3226%
6	0.026000001	0.0288	11.1538%	0.0253	2.3077%
7	0.029999999	0.0318	6%	0.0311	4%
8	0.027000001	0.0286	6.2963%	0.028	7.4074%
9	0.030999999	0.0322	3.871%	0.0320	3.2258%
10	0.033	0.0333	0.9091%	0.0324	1.8182%
11	0.037	0.0352	4.8649%	0.0364	1.3514%
12	0.037999999	0.0364	4.2105%	0.0344	9.2105%
13	0.029999999	0.0311	4%	0.0311	4%
14	0.030999999	0.0317	2.2581%	0.0299	3.2258%
15	0.037	0.0342	7.5676%	0.0368	0.2703%
16	0.029999999	0.0303	1%	0.0286	4.3333%
17	0.034000002	0.0313	7.9412%	0.0315	7.3529%
18	0.029999999	0.0326	8.6667%	0.0297	0.6667%
19	0.028999999	0.0292	0.6897%	0.0289	0%
20	0.030999999	0.0313	0.9677%	0.0322	4.1935%
21	0.028999999	0.0319	10%	0.0297	2.7586%
22	0.035999998	0.03339	7.2222%	0.0346	3.8889%
23	0.026000001	0.0271	4.2308%	0.0270	3.8462%
24	0.033	0.0329	0.303%	0.0303	8.1818%

in the PSO-BP model substantially improved the predictive capability, increasing the R^2 to 0.8098 and reducing the RMSE to 0.0014 mg/L. Ultimately, the dual-optimization PSO-Adam-BP model achieved the most outstanding accuracy, reaching a remarkable R^2 of 0.9351 with impressively low absolute errors, specifically an RMSE of 0.0008 mg/L and a MAE of 0.0006 mg/L.

In order to intuitively judge the total phosphorus concentration inversion effect of the three models, the predicted values of the above three models were compared with the measured values. The results are shown in Fig. 9.

It can be seen from the comparison result diagram that the total phosphorus concentration based on Sentinel-2 remote sensing data using the PSO-Adam-BP model is closer to the measured value in terms of fitting degree, indicating that the PSO-Adam-BP model is superior to the traditional BP neural network model and the PSO-BP neural network model in terms of accuracy, stability, and robustness. The BP neural network model optimized by PSO-Adam has a better effect on the inversion of total phosphorus concentration.

Broader Comparisons with State-of-The-Art Machine Learning Models

To further validate the proposed PSO-Adam-BP framework, broader comparisons were conducted against widely-adopted models referenced in literature [10, 11], including PLSR, Random Forest (RF), XGBoost, and Support Vector Machine (SVM). All models were evaluated on the identical augmented dataset to ensure fairness. The performance metrics are summarized in Table 7.

As shown, the linear PLSR model yielded a poor R2 of 0.1196, failing to capture the complex non-linear relationships between multispectral features and total phosphorus concentrations. Non-linear and

Table 6. Comparison table of three levels of precision.

Model	R^2	RMSE (mg/L)	MAE (mg/L)
Standard BP	0.6881	0.001836	0.001523
PSO-BP	0.8098	0.001434	0.001106
PSO-Adam-BP	0.9351	0.000838	0.000649

ensemble models performed considerably better, with R^2 values reaching 0.8382 for RF, 0.8795 for XGBoost, and 0.8821 for SVM, yet none exceeded the 0.90 threshold. In contrast, the proposed PSO-Adam-BP model significantly outperformed all benchmarks, achieving the highest R^2 of 0.9351 and the lowest absolute errors, specifically an RMSE of 0.0008 mg/L and a MAE of 0.0006 mg/L. This confirms that our hybrid optimization strategy effectively overcomes the limitations of traditional machine learning for complex water quality inversion.

Statistical Validation and Overfitting Discussion

To rigorously assess the model's generalization capability and mitigate the potential bias of a single random data split, a 5-fold cross-validation was explicitly conducted on the entire dataset. The proposed PSO-Adam-BP model achieved an average cross-validation R^2 of 0.9309, an average RMSE of 0.000781 mg/L, and an average MAE of 0.000560 mg/L across the five folds. The minimal variance between the single-split test R^2 of 0.9351 and the rigorous 5-fold cross-validation average demonstrates the exceptional stability of the model, proving that the high inversion accuracy is inherently robust and not dependent on a specific data partition.

Furthermore, given the relatively small sample size intrinsic to complex water quality sampling, the risk of model overfitting was a primary consideration during our architectural design. To systematically mitigate overfitting and prevent the network from merely memorizing the training data, three key strategies were implemented and evaluated. First, Dropout layers were integrated into the deep neural network by randomly discarding 20% of neurons during training, forcing the model to learn robust and redundant feature representations rather than relying on specific pathways. Second, L2 regularization with a weight decay of 1e-4 was applied within the Adam optimizer to penalize excessively large weights and control model complexity. Finally, the rigorous 5-fold cross-validation results, as illustrated by the comprehensive scatter plot in Fig. 10, unequivocally confirmed that the predictive performance on unseen data remains highly consistent with the training performance. Through these combined mechanisms, the proposed dual-optimization framework successfully overcomes the overfitting bottleneck, providing a highly reliable and reproducible inversion tool for practical total phosphorus monitoring in complex aquatic environments like Baiyangdian Lake.

Table 7. Comprehensive performance comparison among various state-of-the-art predictive models.

Model	R^2	RMSE (mg/L)	MAE (mg/L)
PLSR	0.1196	0.003084	0.002438
RF	0.8382	0.001322	0.00107
XGBoost	0.8795	0.001141	0.000678
SVM	0.8821	0.001129	0.001049
PSO-Adam-BP	0.9351	0.000838	0.000649

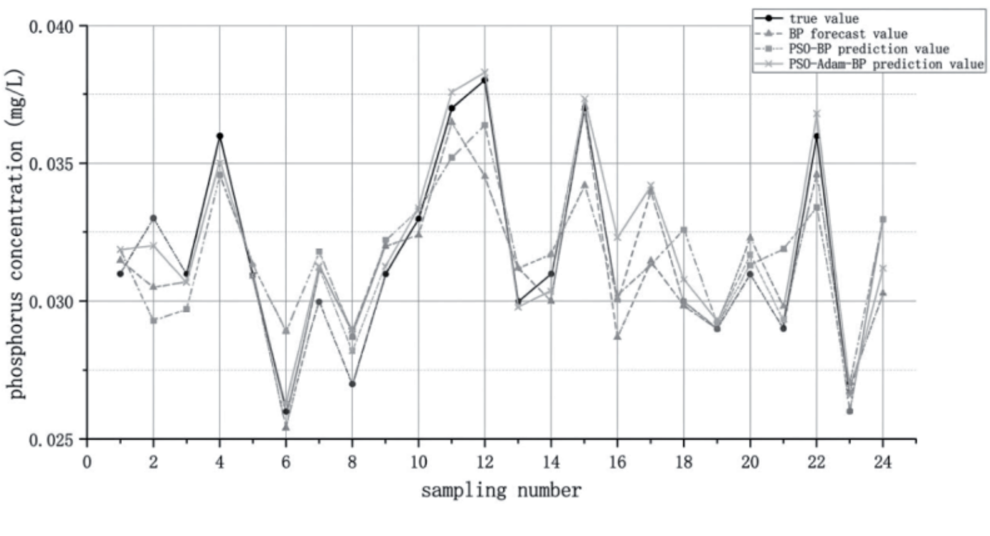

Fig. 9. Comparison results of three models.

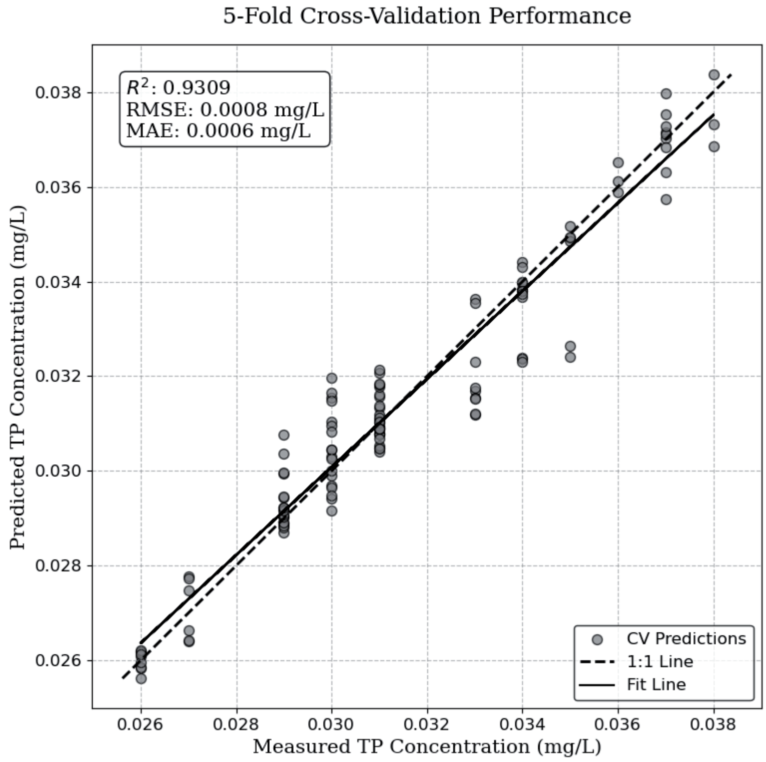

Fig. 10. 5-fold cross-validation scatter plot.

Discussion on Model Interpretability and Limitations

The superiority of the PSO-Adam-BP framework fundamentally stems from its ability to capture highly non-linear optical relationships. Since total phosphorus is optically inactive, it must be inferred indirectly via optically active proxies. Traditional models often become trapped in local optima within these complex spectral spaces. The proposed dual-optimization strategy explicitly solves this: PSO performs a global search for optimal initial weights, while Adam executes precise gradient fine-tuning, successfully deciphering the subtle non-linear variations of TP.

Despite these advantages, inherent limitations in remote sensing data remain. First, Sentinel-2's 10-20 m spatial resolution may be insufficient for extremely small water bodies due to mixed-pixel effects. Second, the low surface reflectance of water makes it highly susceptible to residual atmospheric interference. To address these challenges, future work will explore hyperspectral remote sensing. By providing continuous, narrow-band spectral profiles, hyperspectral data will enable the capture of much finer absorption features, promising higher precision for the inversion of non-optical parameters like TP.

Furthermore, regarding the model's transferability to other inland lakes beyond Baiyangdian Lake, the underlying architecture of the PSO-Adam-BP framework is highly adaptable. While the current model weights are calibrated specifically for the optical properties of Baiyangdian Lake, the framework can serve as a robust pre-trained base model. For future applications in lakes with different trophic states or optical characteristics, researchers can employ transfer learning techniques – fine-tuning the network using a small amount of local sampled data – thereby efficiently deploying the model to new regions without the need for extensive retraining from scratch.

Conclusions

Based on Sentinel-2 remote sensing images and measured total phosphorus concentration data in water bodies, this paper constructed a PSO-Adam-BP neural network model based on full-band features and feature engineering, which improved the accuracy of total phosphorus concentration inversion in Baiyangdian Lake in Xiongan New Area. The research conclusions are as follows:

(1) A combined feature signature was constructed using the full Sentinel-2 multispectral band and constructed water characteristic indices (NDTI, B5/B6 ratio, shortwave infrared composite features, etc.). The model constructed based on this combined signature exhibited high accuracy, indicating that this combined signature effectively reflects the relationship with total phosphorus in water.

(2) A PSO-Adam-BP neural network model was proposed. This study combines the global optimization advantages of PSO with the nonlinear fitting capabilities of BP neural networks. The Adam algorithm is used for quadratic weight optimization. This solves the

problem that traditional BP neural networks are prone to falling into local optimality, significantly improving the convergence speed and prediction accuracy of the BP neural network model.

Based on this study, subsequent research could explore the relationship between hyperspectral data and measured samples. Furthermore, hybrid modeling could be expanded to incorporate measured sample data and physical mechanism-driven approaches, continuously enhancing the interpretability and generalizability of the model, providing scientific support for watershed water quality monitoring and ecological restoration.

Acknowledgments

This study was financially supported by the S&T Program of Hebei (254Z4202G), the Research on Water Eutrophication Monitoring Method Based on Convolutional Neural Network (YKY-2025-122), the Hebei Province Natural Science Foundation - Young Scientific Research Fund Project (Category C) (D2025409010), the Science and Technology Research Projects of Higher Education Institutions in Hebei Province (QN2023261), the Doctoral Research Start-up Fund of North China Institute of Aerospace Engineering (BKY-2022-07), and the Technology Research and Development Program of China Construction First Group Corporation (KJYF-2022-12). We also extend our sincere gratitude to our supervisor in the research team for their invaluable assistance in dataset collection and guidance throughout the manuscript preparation. Additionally, we sincerely appreciate the anonymous reviewers for their insightful comments and dedicated efforts.

AI Usage Disclosure Statement

During the preparation of this manuscript, the authors used Gemini solely for the purpose of language editing and grammar correction to improve the readability of the English text. After using this tool, all authors rigorously reviewed and verified the content. The authors take full and final responsibility for the scientific findings, data accuracy, and the originality of this publication.

Conflicts of Interest

The authors declare no conflict of interest.

References

1. ZHANG Y., LI M., DONG J., YANG H., VAN ZWIETEN L., LU H., ALSHAMERI A., ZHAN Z., CHEN X., JIANG X., XU W., BAO Y., WANG H. A Critical Review of Methods for Analyzing Freshwater Eutrophication. Water, **13** (2), 225, **2021**.
2. AKHTAR N., SYAKIR ISHAK M.I., BHAWANI S.A., UMAR K. Various Natural and Anthropogenic Factors Responsible for Water Quality Degradation: A Review. Water, **13** (19), 2660, **2021**.
3. SAVIC R., STAJIC M., BLAGOJEVIĆ B., BEZDAN A., VRANESEVIC M., NIKOLIĆ JOKANOVIĆ V., BAUMGERTEL A., BUBALO KOVAČIĆ M., HORVATINEC J., ONDRASEK G. Nitrogen and Phosphorus Concentrations and Their Ratios as Indicators of Water Quality and Eutrophication of the Hydro-System Danube–Tisza–Danube. Agriculture, **12** (7), 935, **2022**.
4. HOWARTH R.W., CHAN F., SWANEY D.P., MARINO R.M., HAYN M. Role of External Inputs of Nutrients to Aquatic Ecosystems in Determining Prevalence of Nitrogen vs. Phosphorus Limitation of Net Primary Productivity. Biogeochemistry, **154** (2), 293, **2021**.
5. HABYARIMANA J.L., MA J., NYIRANSENGIYUMVA C., TIAN W.Q., CAI Y.Q., TWAGIRAYEZU G., DENG Y. Critical Review on Operation Mechanisms to Recover Phosphorus from Wastewater via Microbial Procedures Amalgamated with Phosphate-rich in Side-stream to Enhance Biological Phosphorus Removal. Biocatalysis and Agricultural Biotechnology, **45**, 102484, **2022**.
6. BRENCKMAN C.M., PARAMESWARAPPA JAYALAKSHMAMMA M., PENNOCK W.H., ASHRAF F., BORGAONKAR A.D. A Review of Harmful Algal Blooms: Causes, Effects, Monitoring, and Prevention Methods. Water, **17** (3), 1980, **2025**.
7. ANABTAWI H.M., LEE W.H., AL-ANAZI A., MOHAMED M.M., ALY HASSAN A. Advancements in Biological Strategies for Controlling Harmful Algal Blooms (HABs). Water, **16** (2), 224, **2024**.
8. ZAINURIN S.N., WAN ISMAIL W.Z., MAHAMUD S.N.I., ISMAIL I., JAMALUDIN J., ARIFFIN K.N.Z., WAN AHMAD KAMIL W.M. Advancements in Monitoring Water Quality Based on Various Sensing Methods: A Systematic Review. International Journal of Environmental Research and Public Health, **19** (21), 14080, **2022**.
9. CHEN L., LIU L., LIU S., SHI Z., SHI C. The Application of Remote Sensing Technology in Inland Water Quality Monitoring and Water Environment Science: Recent Progress and Perspectives. Remote Sensing, **17** (4), 667, **2025**.
10. JANGA B., ASAMANI G.P., SUN Z., CRISTEA N. A Review of Practical AI for Remote Sensing in Earth Sciences. Remote Sensing, **15** (16), 4112, **2023**.
11. DENG Y., ZHANG Y., PAN D., YANG S.X., GHARABAGHI B. Review of Recent Advances in Remote Sensing and Machine Learning Methods for Lake Water Quality Management. Remote Sensing, **16** (22), 4196, **2024**.
12. CHEN B., MU X., CHEN P., WANG B., CHOI J., PARK H., XU S., WU Y., YANG H. Machine Learning-based Inversion of Water Quality Parameters in Typical Reach of the Urban River by UAV Multispectral Data. Ecological Indicators, **133**, 108434, **2021**.
13. LIANG Y., YIN F., XIE D., LIU L., ZHANG Y., ASHRAF T. Inversion and Monitoring of the TP Concentration in Taihu Lake Using the Landsat-8 and Sentinel-2 Images. Remote Sensing, **14** (24), 6284, **2022**.
14. ZHENG S., MA F., ZHOU J., DU C. Monitoring of Total Phosphorus in Urban Water Bodies Using Silicon

Crystal-Based FTIR-ATR Coupled with Different Machine Learning Approaches. Water, **16** (17), 2479, **2024**.
15. SONG K., LI L., LI S., TEDESCO L., HALL B., LI L. Hyperspectral Remote Sensing of Total Phosphorus (TP) in Three Central Indiana Water Supply Reservoirs. Water, Air, & Soil Pollution, **223** (4), 1481, **2011**.
16. ZHOU Y., YANG W., HU M., LI J., LIU X. Research on Remote Sensing Inversion of Total Phosphorus in East Juyan Lake Based on Machine Learning. Hydrology, **12** (11), 299, **2025**.
17. SUN Z., GUO L., TAO Z., LI Y., ZHAN Y., LI S., ZHAO Y. Water Quality Inversion Framework for Taihu Lake Based on Multilayer Denoising Autoencoder and Ensemble Learning. Remote Sensing., **16** (24), 4793, **2024**.
18. KYRIAZOS T., POGA M. Application of Machine Learning Models in Social Sciences: Managing Nonlinear Relationships. Encyclopedia, **4** (4), 1790, **2024**.
19. DU K.-L., LEUNG C.-S., MOW W.H., SWAMY M.N.S. Perceptron: Learning, Generalization, Model Selection, Fault Tolerance, and Role in the Deep Learning Era. Mathematics, **10** (24), 4730, **2022**.
20. CAI Y., ZHANG P., WANG Q., WU Y., DING Y., NABI M., FU C., WANG H., WANG Q. How Does Water Diversion Affect Land Use Change and Ecosystem Service: A Case Study of Baiyangdian Wetland, China. Journal of Environmental Management, **344**, 118558, **2023**.
21. HE S., LIN M., SHI L., CHEN D. Occurrence, Distribution and Ecological Risk Assessment of Contaminants in Baiyangdian Lake, China. Water, **14** (21), 3352, **2022**.
22. YANG Y., ZHANG D., LI X., WANG D., YANG C., WANG J. Winter Water Quality Modeling in Xiong'an New Area Supported by Hyperspectral Observation. Sensors, **23** (8), 4089, **2023**.
23. HAN Y.L., BU H.M. The Impact of Climate Change on the Water Quality of Baiyangdian Lake (China) in the past 30 years (1991-2020). Science of The Total Environment, **870**, 161957, **2023**.
24. WANG G., LV C., GU C., YU Y., YANG Z., ZHANG Z., TANG C. Pollutants Source Assessment and Load Calculation in Baiyangdian Lake Using Multi-Model Statistical Analysis. Water, **14** (21), 3386, **2022**.
25. Water Quality of Baiyangdian Lake in North China Improves After Protection Activities. Available online: https://english.news.cn/20240509/672f61c7b3cf4c7586cb3927e4fef5ac/c.html (accessed on 9 May **2024**).
26. PARK J., KHANAL S., ZHAO K., BYUN K. Remote Sensing of Chlorophyll-a and Water Quality over Inland Lakes: How to Alleviate Geo-Location Error and Temporal Discrepancy in Model Training. Remote Sensing, **16** (15), 2761, **2024**.
27. YUAN X., WANG S., FAN F., DONG Y., LI Y., LIN W., ZHOU C. Spatiotemporal Dynamics and Anthropologically Dominated Drivers of Chlorophyll-a, TN and TP Concentrations in the Pearl River Estuary based on Retrieval Algorithm and Random Forest Regression. Environmental Research, **215**, 114380, **2022**.
28. WANG J.F., STEIN A., GAO B.B., GE Y. A Review of Spatial Sampling. Spatial Statistics, **2** (1) 1-14, **2012**.
29. ZENG H., HE X., BAI Y., GONG F., WANG D., ZHANG X. Design and Construction of UAV-Based Measurement System for Water Hyperspectral Remote-Sensing Reflectance. Sensors, **25** (9), 2879, **2025**.
30. RENOSH P.R., DOXARAN D., KEUKELAERE L.D., GOSSN J.I. Evaluation of Atmospheric Correction Algorithms for Sentinel-2-MSI and Sentinel-3-OLCI in Highly Turbid Estuarine Waters. Remote Sensing, **12** (8), 1285, **2020**.
31. EL BILALI A., TALEB A., BAHLAOUI M.A., BROUZIYNE Y. An Integrated Approach based on Gaussian Noises-based Data Augmentation Method and AdaBoost Model to Predict Faecal Coliforms in Rivers with Small Dataset. Journal of Hydrology, **599**, 126510, **2021**.
32. GASCON F., BOUZINAC C., THÉPAUT O., JUNG M., FRANCESCONI B., LOUIS J., LONJOU V., LAFRANCE B., MASSERA S., GAUDEL-VACARESSE A., LANGUILLE F., ALHAMMOUD B., VIALLEFONT F., PFLUG B., BIENIARZ J., CLERC S., PESSIOT L., TRÉMAS T., CADAU E., DE BONIS R., ISOLA C., MARTIMORT P., FERNANDEZ V. Copernicus Sentinel-2A Calibration and Products Validation Status. Remote Sensing., **9** (6), 584, **2017**.